J. Synchrotron Rad. (1996). **3**, 272–281

Design of an X-ray Phase-Plate Analyzer to Measure the Circular Polarization Rate of a Helical Undulator Source

José Goulon,[a] Cécile Malgrange,[b] Carlos Giles,[a] Claus Neumann,[a] Andrej Rogalev,[a] Eric Moguiline,[a] François De Bergevin[a,c] and Christian Vettier[a]

[a]*European Synchrotron Radiation Facility, BP 220, F-38043 Grenoble CEDEX, France,* [b]*Laboratoire de Minéralogie-Cristallographie, Associé au CNRS, Universités Paris VI & Paris VII, Case 115, Tour 16, 4 Place Jussieu, F-75252 Paris CEDEX 05, France, and* [c]*Laboratoire de Cristallographie, BP 166, F-38043 Grenoble CEDEX, France*

(*Received 13 February 1996; accepted 30 May 1996*)

A quarter-wave plate made of a *ca* 16 μm-thick silicon single crystal was used at energies as low as 2.8 keV to convert circularly polarized photons into linearly polarized photons. Coupled to a linear polarimeter, this quarter-wave plate enabled the characterization of the circular polarization rate of the radiation emitted by one of the ESRF helical undulators, Helios-I. The measured value (*ca* 97%) is in good agreement with theoretical predictions. Special attention was paid to the alignment procedures of all relevant optical components of the beamline.

Keywords: transmission X-ray phase plates; X-ray polarimeters; helical undulator; alignment procedures.

1. Introduction

X-ray phase plates exploit the double birefringence of either perfect or mosaic crystals under the conditions of Bragg diffraction (Molière, 1939; Hart & Lang, 1965). Skalicky & Malgrange (1972) were the first to show experimentally that all four branches of the dispersion surface could be excited and that, under proper conditions, linearly polarized incident radiation could be converted into elliptically polarized light. This is possible because there is a finite difference $(n_\sigma - n_\pi)$ between the indices of refraction of the σ and π components of the electric field, perpendicular and parallel to the plane of diffraction, respectively. A 90° phase shift can thus be introduced between the σ and π components simply by properly matching the X-ray path inside the crystal. The difference $(n_\sigma - n_\pi)$ depends on the angular offset $\Delta\Theta$ from the Bragg condition: whereas rather dramatic variations of this quantity are expected inside the reflection domain, a smooth dependence is predicted when the angular offset $\Delta\Theta$ exceeds the Darwin width. This is why the latter regime appears most attractive for experiments with X-ray phase plates. Furthermore, since $(n_\sigma - n_\pi)$ is identical for both the reflected and forward-diffracted waves, it is possible to induce phase retardations (i) either with the reflected beam or the transmitted beam in a Laue geometry, and (ii) in the transmitted beam using the Bragg geometry.

Two groups of applications have been developed with X-ray phase plates:

(i) The first group concentrates on the *transformation* of the polarization state of a polarized source of X-ray photons. A typical problem is to transform linearly polarized light into circularly polarized light with a quarter-wave plate (QWP) (Dmitrienko & Belyakov, 1980; Belyakov & Dmitrienko, 1989; Hirano, Izumi, Ishikawa, Annaka & Kikuta, 1991; Hirano *et al.*, 1992; Hirano, Ishikawa & Kikuta, 1995; Ishikawa, Hirano & Kikuta, 1991; Giles *et al.*, 1993, 1994*a*,*b*, 1995*a*,*b*; Lang & Srajer, 1995). Alternatively, it may be desirable to rotate the linear polarization by 90° using a half-wave plate, *e.g.* to transform a horizontal transverse polarization into a vertical transverse polarization (Giles *et al.*, 1993; Giles, Vettier *et al.*, 1995).

(ii) The second group of applications deals with the characterization of the polarization state of synchrotron radiation sources. At optical wavelengths it is well known that the polarization state of a source can be fully determined by combining a quarter-wave plate with a linear polarimeter. The availability of X-ray phase plates now makes it possible to extend the same concept in the X-ray range. If the different components of the Stokes vector are measured independently, then the degree of polarization of the source can be determined. Note that in all the experiments reported so far the quarter-wave plate was illuminated with a highly collimated monochromatic beam (Ishikawa *et al.*, 1991; Ishikawa, Hirano, Kanzaki & Kikuta, 1995; Giles *et al.*, 1993; Giles, Vettier *et al.*, 1995).

In the present study the goal was to estimate the circular polarization rate of the radiation emitted by Helios-I, a new type of helical undulator developed at the ESRF (Elleaume, 1994). To be strictly characteristic of the source, such measurements need to be carried out *upstream* with respect to the double-crystal monochromator because the polarization transfer function of the latter optical component becomes very poor at Bragg angles approaching 45° (Malgrange, Carvalho, Braicovich & Goulon, 1991). The circular po-

larization rate of the source is indeed directly relevant for a few experiments exploiting the wide-band undulator radiation, *e.g.* dichroism in high-resolution fluorescence spectra or in reflectivity. The circular polarization rates downstream of the monochromator can be measured with a different experimental set-up that will not be discussed here.

What makes the experiment described below original is that (*a*) we have inserted the quarter-wave plate into a polychromatic section, (*b*) the double-crystal monochromator, which is equipped with a pair of Si 111 crystals, was acting as a linear polarimeter at an energy of *ca* 2.8 keV, and (*c*) at such a low energy the operation of a phase plate becomes more difficult due to high absorption losses.

It is the aim of the present paper to detail various experimental aspects of our measurements and to report on the first analyses which confirm that Helios-I produces intense beams of X-rays with high circular polarization rates.

2. Instrumentation

2.1. *Helical undulator sources*

Two helical undulators (Helios-I and Helios-II) are inserted into the straight section ID12 of the ESRF storage ring (Elleaume, 1994). They have the same design concept in common: horizontal (B_x) and vertical (B_z) magnetic fields with strictly the same spatial periodicity (λ_u) are generated by two planar arrays of permanent magnets assembled in two magnetic jaws fixed to rigid girders. There are three independent degrees of freedom: an axial translation (T_y) of the upper girder along the beam direction induces a variation of the 'phase' (φ) between the horizontal and vertical fields and enables the user to change the ellipticity of the undulator radiation from linear ($\varphi = 0$) to circular right ($\varphi = +\pi/2$) or circular left ($\varphi = -\pi/2$). The corresponding amplitude or the translation is simply $T_y = 0, \pm\lambda_u/4$; vertical translations (T_z) of each individual girder allow us not only to shift the peak energy of the undulator spectrum but also to change the ratio $\rho = B_x/B_z$ which has a direct effect on the relative intensities of higher harmonics, as shown by Elleaume *et al.* (1991). It should be borne in mind that circular polarization can only be obtained for $\rho = 1$ and a careful adjustment of the half gaps T_z (B_x) and T_z (B_z) is critical to maximize the circular polarization rates. For elliptical polarization ($\rho \neq 1$), varying ρ will both rotate the long axis of polarization and change the ellipticity.

The magnetic periods of Helios-I (λ_u = 85 mm) and Helios-II (λ_u = 52 mm) have been specified so as to cover complementary (but also overlapping) spectral ranges with the two sources. With a 'standard' first-generation ID vacuum chamber, the minimum half gaps were restricted to 10 mm and the spectral lines of the first harmonic peaked at *ca* 0.57 keV for Helios-I and 3.06 keV for Helios-II. The spectral range has recently been shifted down to low energy using a narrow-gap vacuum chamber. With the new chamber Helios-II can deliver a satisfactory supply of photons at 2.8 keV but there is no hope of satisfying the condition $B_x/B_z = 1$, so that the emission is at best elliptically polarized. Helios-I is *a priori* a more attractive source to conduct the experiments described below because the condition $B_x/B_z = 1$ can be satisfied for T_z (B_x) = 20.5 mm and T_z (B_z) = 29.14 mm: under such conditions the first harmonic was found to peak at 2.836 keV. The phase was set to $\varphi = \pi/2$, *i.e.* $T_y = +\lambda_u/4$ = 21.25 mm.

There is another peculiarity associated with Helios-I: it combines two segments (Helios-I*A* and Helios-I*B*) each consisting of only nine magnetic periods, plus a 'magnetic chicane' which perturbs the direction of injection of the electrons in both segments (Elleaume, 1994). As a consequence, the axes of emission of Helios-I*A* and Helios-I*B* are deflected in a symmetrical way with respect to the direction of injection of the downstream undulator Helios-II: although the 'kick' angle is as small as 200–340 µrad, this is large enough to allow the three beams of Helios-I*A*, Helios-II and Helios-I*B* to be fully separated at the beamline front end, *i.e.* at 26.5 m from the middle source point of Helios-I. The magnetic design yields reversed 'phases' for Helios-I*A* and Helios-I*B* which therefore deliver two beams with strictly opposite circular polarization. One may worry about an eventual contamination of the Helios-II radiation by the Gaussian tails of the two side beams of Helios-I which may contribute on-axis to some residual unpolarized background. Fortunately, Helios-I and Helios-II usually have completely different emission spectra and it has been checked that the maximum level of contamination of the central beam of Helios-II did not exceed a few percent of its own intensity. At very low energy we found that the two beams of Helios-I were themselves slightly contaminated by the synchrotron radiation due to the leak fields of the adjacent bending magnets. This can be checked by monitoring the residual intensity while keeping open the gaps of both Helios-I and Helios-II; the residual signal is small.

2.2. *Optics and detectors*

Two different spectrometers are available at the ESRF for polarization-dependent X-ray spectroscopy:

(i) Spectra requiring low excitation energies ($E \leq 1.7$ keV) are preferably recorded with a 'Dragon'-type grating spectrometer installed on a side-branch beamline (referred to as ESRF BL26 or 'ID12B'). This side-branch has much in common with the AT&T Bell Laboratories beamline (Chen, 1987; Chen & Sette, 1989). It consists of a dispersive section (*i.e.* a spherical grating with movable entrance–exit slits) coupled to the undulator source by high-quality Kirkpatrick–Baez reflective optics.

(ii) Experiments at higher excitation energy all take place on the straight-branch beamline (ESRF BL6 or 'ID12A') which makes use of crystal optics. In Fig. 1 we have reproduced a schematic layout of this beamline in its present configuration. We have to admit that neither the four-mirror device (4M-D) nor the vertically focusing optics (VF-2M) were ready by the time of the early experiments reported

here. It may be worth emphasizing that BL6 and BL26 are now operated full time in parallel except when there is a very strong request to use Helios-I on BL6, as in the present case.

The multi-pinhole device was set up to extract one single beam (*i.e.* beam 'B') of Helios-I through a 1 × 1 mm pinhole located 26.6 m from the source. The collimation of the beam was furthermore increased in the vertical plane using the secondary slits located at 35.5 m and closed down to 0.3 mm. The collimation of the X-ray beam was then better than 17 μrad in the vertical plane and 75 μrad in the horizontal plane. The quarter-wave-plate chamber was inserted in the so-called 'white beam' experimental station located upstream of the double-crystal monochromator, which is located at 39.3 m from the source point.

The fixed-exit two-crystal monochromator was manufactured for the ESRF by KoHzu Seiki Co. (Japan). This is an upgraded, UHV-compatible version of the double-cam instrument initially described by Matsushita, Ishikawa & Oyanagi (1986). Particularly useful for the present application is the implementation of an axial rotation R_s (±48°) of the whole instrument around the direction of the incident X-ray beam. The axis of the R_s rotation is stable within ±10 μm on scanning the Bragg angle. Self-regulated digital piezos with nanometric resolution have been purchased from Queensgate Instruments Ltd. (UK) and are used mostly to control the parallelism of the two crystals. We have the capability to refine the stability of the exit beam below a couple of micrometers but there was no need for this in the present experiment. The temperature of each individual crystal can be stabilized to ±0.2 K at any desired temperature from room temperature down to 140 K: our cryogenic cooling system exploits a continuous flow of cold He gas in a closed-loop circuitry with integrated heat exchangers. Commissioning tests have shown that the intrinsic reproducibility or angular stability of the maximum of a rocking curve during an EXAFS scan or after two consecutive EXAFS scans was better than 0.14 arcsec. For large-amplitude R_s (±48°) rotations, the observed angular stability of the rocking curve was of the order of 0.3 arcsec or even better. As detailed in *Appendix A*1, further geometrical effects have to be taken into account when using the $R_s(\chi)$ rotations:

(i) As the direction of the incident X-ray beam never coincides perfectly with the true axis of the rotation R_s, large-amplitude R_s rotations are expected to induce tiny shifts in the energy calibration (*Appendix A*1).

(ii) Symmetrical displacements of the exit beam are predicted for $R_s(\pm\chi)$ rotations; in reality, small asymmetries are observed whenever the parallelism of the second crystal is not perfectly adjusted. This turns out to be a sensible alignment criterion (*Appendix A*2).

Intensity and beam-position monitors all based on *pnn*[4] photodiodes operated in the photoconductive mode are

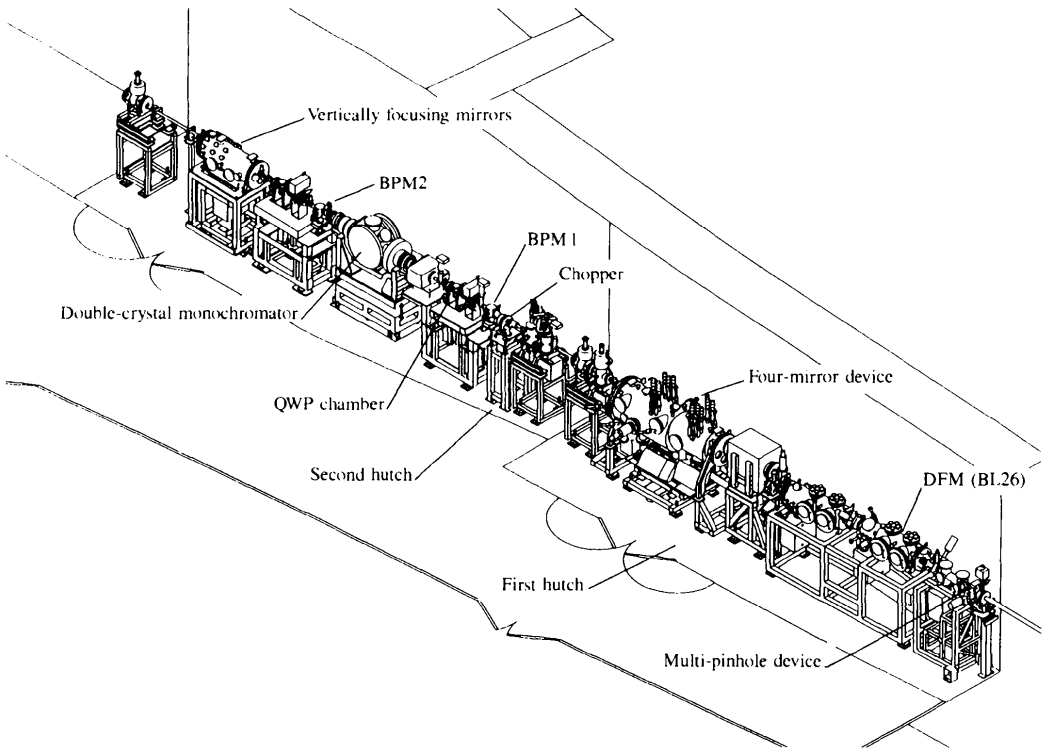

Figure 1
Schematic layout of the ESRF BL6 (ID12A). For the sake of simplicity, the side-branch (BL26/ID12B) is not represented beyond the deflecting mirrors (DFM). In the experiment reported here, the four-mirror device and the vertically focusing mirrors were not available. The location of the beam-position monitors in the second hutch is indicated.

available at various places of the beamline. The incident beam is chopped at a rather low frequency (*e.g.* 72 Hz) and the a.c.-modulated analogue signal delivered by low-noise electrometers is fed into home-made multi-channel digital lock-in boards: this proved to be most efficient for eliminating any residual dark-current noise (Gauthier *et al.*, 1995). The beam-position monitors have a typical resolution of ±1 μm in the vertical or horizontal positions of both the 'white' beam and the monochromatic beam.

2.3. *Mechanical design of the phase-plate polarimeter*

This instrument consists primarily of a UHV-compatible stainless-steel chamber (VAC) which has the shape of a six-way cross directly machined from a metal block in order to meet our tight geometrical specifications (Fig. 2). Four ports are equipped with CF38 flanges, and two ports with CF63 flanges: fixed onto one such large CF63 flange is the high-precision goniometer head. A major feature of the phase-plate chamber is that it can be rotated around the beam axis just like the monochromator: this rotation, hereafter denoted as $r_s(\xi)$, can easily cover the full range of interest, *i.e.* ±90°. The mechanical design is based on a high-precision playless helical wormscrew (Zahnradfabrik OTT) actuated by a stepper motor that has its own reductor and built-in optical encoder so that the actual step size in the angular positioning is 0.03° (108 arcsec): this is good enough for the present application. Two differentially pumped rotatable platforms (RNN-150 from Thermoionics Vacuum Products) equipped with spring-loaded teflon–graphite seals make the r_s rotation fully compatible with the UHV environment of the experimental station. Bakeout of the whole chamber was not even needed to reach the desired vacuum ($\leq 10^{-8}$ mbar) within a few hours.

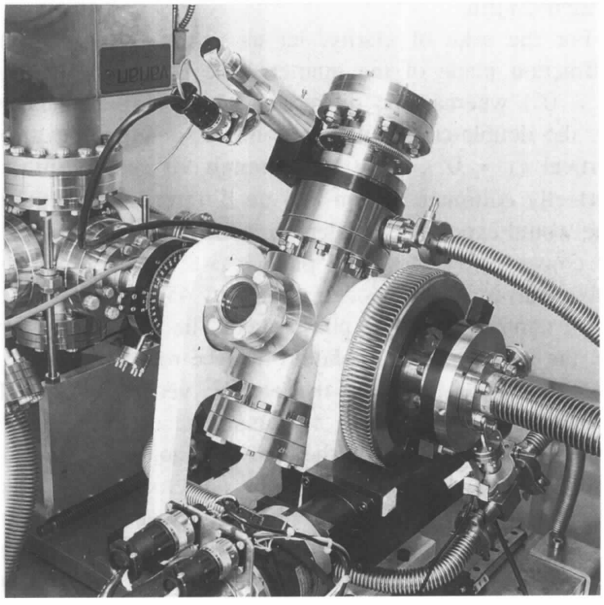

Figure 2
The quarter-wave-plate UHV chamber. The goniometer head (GOH), the playless helical wormscrew and the differentially pumped rotatable platforms are apparent.

The rotation $r(\theta_{Bp})$ of the phase plate in the goniometer head is performed using two-stage mechanics:

(i) Large-amplitude rotations (up to 360°) are achieved with a differentially pumped high-precision rotary drive (DPRF-55 from VG-Instruments) actuated with a vibration-free d.c. motor (Minimotors SA) again combined with an optical encoder. The accuracy of these mechanics does not exceed 20 arcsec and is not suitable for an accurate setting of the Bragg angle. It is, however, extremely useful for Bragg scans over a wide angular range.

(ii) A compact mechanical system was designed to provide a very precise and highly reproducible rotation over a useful range of ±275 arcsec. As illustrated in Fig. 3, it combines flexure hinges and a UHV-compatible self-sensing digital piezo translator from Queensgate Instruments. This DPT-C translator associated with its controller AX301 has nanometric resolution. Laser interferometry measurements were performed to generate and store a calibration chart in the computer memory. Absolute reproducibility is in the range of 0.5 arcsec.

The whole instrument is mounted on a standard experimental table with remotely controlled vertical (T_z) and horizontal (T_x) translations. The crystal phase plate was cut and thinned down in the ESRF crystal laboratory. It can be observed from Fig. 3 that an S-shape was retained in order to minimize the small constraints generated by the crystal clamping. Etching techniques were used to reduce the crystal thickness down to *ca* 16 ± 3 μm only in a limited area exposed to the X-ray beam. The crystal was cut with the surface parallel to the Si 111 reflecting planes. Although the crystal holder was water-cooled, the heat load turned out to be high enough to cause some permanent deformation of the thin crystal: this resulted in a progressive (unfortunately irreversible) broadening with time of the transmission profiles, these effects becoming significant after several days of operation.

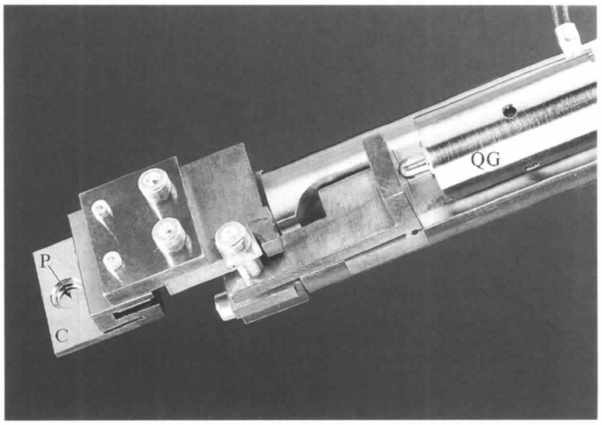

Figure 3
The quarter-wave-plate holder. Note the S-shape of the thick silicon crystal (*C*) which is used to minimize the stress in clamping. The etched zone with reduced thickness (*P*) is apparent. Less apparent is the monolithic flexure hinge system which is used to adjust the orientation of the crystal. The digital piezo from Queensgate Instruments is also shown (*QG*).

3. Experiment

3.1. *Operation of a phase plate at low energy*

The phase shift Φ between the σ and π components of the electric field inside the crystal is defined by

$$\Phi = (2\pi/\lambda)(n_\sigma - n_\pi)t, \quad (1)$$

where λ is the wavelength in the vacuum and t (hereafter called the effective thickness) is the X-ray path length. According to the dynamical theory of X-ray diffraction, this phase shift can be given a simple expression *far from the total reflection regime*:

$$\Phi = (-\pi/2)[r_e^2\lambda^3 \,\mathrm{Re}(F_h F_{\bar{h}}) \sin(2\theta)t]/[(\pi V)^2(\theta - \theta_0)]$$
$$= (-\pi/2)At/\Delta\Theta, \quad (2)$$

where r_e is the classical electron radius, V is the volume of the unit cell, and F_h and $F_{\bar{h}}$ are the structure factors of the hkl and $\bar{h}\bar{k}\bar{l}$ reflections, respectively. Let us define θ_B as the angle of incidence satisfying the Bragg condition at a given wavelength, and θ_0 as the angle of incidence of a wave of identical energy exciting the centre of the reflection profile which takes into account the small correction for refraction. The quantity denoted hereafter as $\Delta\Theta$ (= $\theta - \theta_0$) will be referred to as the *angular offset* of the incident wave. Equation (2) allows us to predict that the phase shift will decrease on increasing the angular offset and that its sign may be reversed by selecting either positive or negative values of $\Delta\Theta$. Equation (2) also shows that the phase shift is proportional to the product of the effective thickness t by some characteristic factor A, which depends mainly on the selected crystal. It is obviously desirable to keep the effective thickness small in order to minimize the absorption losses, but the crystal thickness cannot be reduced below realistic limits. It is therefore desirable to maximize A at the desired energy of operation and to satisfy the following criteria for the product At:

$At \geq$ the Darwin width ω_D;

$At \geq$ the angular dispersion of the incident beam ω_0;

$At \geq$ the crystal mosaicity ω_M.

Maximizing A becomes highly desirable whenever the collimation or the monochromaticity of the incident beam are poor. For energy-dispersive circular magnetic X-ray dichroism (CMXD) experiments, the latter considerations are in favour of using diamond 111 phase plates rather than a silicon 220 phase plate, which would also be more absorbing (Giles *et al.*, 1994*a*,*b*). Similar arguments were recently developed to justify the possible use of a mosaic Be phase plate operated with the Be 002 reflection (Giles *et al.*, 1995*a*; Giles, Malgrange, De Bergevin *et al.*, 1995).

In the present experimental configuration we had to include further constraints: (i) the phase plate, being inserted before the monochromator, has to accommodate a rather high heat load of typically 4 W mm^{-2}; (ii) to act as an efficient linear polarimeter the double-crystal monochromator has to be operated at a Bragg angle very close to 45°. The latter condition defines the optimum energy of the experiment depending on which pair of crystals is mounted.

Monochromator:	Si 111	Si 220	Si 311	Si 400	Si 333
Energy (keV):	2.7961	4.5661	5.3542	6.4575	8.38825

By the time of the proposed experiment, the monochromator was equipped with a pair of Si 111 crystals and the measurements had thus to be performed at *ca* 2.8 keV. This immediately ruled out the use of a diamond quarter-wave plate because the lattice parameter of diamond is too small to satisfy the Bragg condition at 2.8 keV. The simplest choice was then to use a thin Si 111 crystal as phase plate. For the preselected undulator gaps, the maximum intensity was found to peak at E = 2.836 keV (θ_B = 44.2°). In order to maximize the transmitted signal we decided to carry out the experiment at this peak energy which (unfortunately) did not correspond strictly to the desired Bragg angle of 45°. Under such conditions, A = 2012 arcsec mm^{-1} and ω_D = 27.0 arcsec. For a 10 μm-thick crystal (*i.e.* t = 14.14 μm), one finds At = 28.4 arcsec, which is close to ω_D. The initially specified thickness of 20 μm was thus a reasonable compromise satisfying the criterion $At \geq \omega_D$. Unfortunately, we never succeeded in obtaining such a thin crystal with a uniform thickness: again we considered that the best strategy was to maximize as much as possible the transmission of the plate by experimenting with the horizontal or vertical translations of the whole chamber. As a consequence, the crystal thickness became an adjustable parameter in our experiment: on the other hand, thickness measurements were not accurate enough and it is simply our *guess* that, locally, the thickness of the plate was typically 16–17 μm with an effective thickness t = 22.6–24 μm.

For the sake of clarity, let us assume next that the diffraction plane of the quarter-wave plate is horizontal (ξ = 0°) whereas the diffraction plane of the analyzer, *i.e.* the double-crystal monochromator, is supposed to be vertical (χ = 0°). With an optimum 90° phase shift, a perfectly collimated beam and no differential absorption, one would expect the incident circularly polarized wave to be converted by the phase plate into a linearly polarized wave with its electric vector rotated by 45° with respect to the π component of the phase plate. The crystal analyzer, *i.e.* the monochromator, should then be rotated by $R_1(\chi$ = ±45°) in order to allow the electric vector to coincide with a pure σ' or a pure π' component of the analyzer. Ideally, in the latter case, the analyzer should not transmit any monochromatic beam and the detector should detect zero intensity. In reality, there is a further complication arising from the fact that, at such low energy, the quarter-wave plate will attenuate the electric field components parallel to the σ and π axes in fairly different proportions. This is illustrated in Fig. 4 which compares the calculated intensities I_σ and I_π transmitted by a 16 μm-thick Si 111 phase plate as a function of the angular offset angle relative

to $\theta_B = 44.2°$ for $E = 2.836$ keV. It is easy to check from equation (2) that a phase shift of +90° will be obtained for an angular offset of $\Delta\Theta = -45.5$ arcsec, so that, according to Fig. 4, the transmitted intensities should be in the ratio $(I_\sigma/I_\pi) \simeq 2.75$. The practical consequence is that the incident circularly polarized wave may still be converted into a linearly polarized wave but the electric vector will now be rotated by a different azimuthal angle α ($\neq 45°$) which is simply defined by the condition:

$$\tan\alpha = (I_\sigma/I_\pi)^{1/2} \simeq 1.66.$$

In turn, the analyzer will have to be rotated by $R_s(\chi = \alpha - 90° = -31°)$ in order to allow the electric vector to again become a pure π' component and allow the transmitted intensity to become zero, or at least minimum. Alternatively, if the diffraction plane of the quarter-wave plate was rotated by $r_s(\xi = +31°)$, then the transmitted intensity should become zero or minimum for $R_s(\chi = 0°)$. In practice, during the experiment, we assumed that the thickness of the plate was 17 μm with the practical consequence that α had a slightly different value (62°). The experiments were then carried out with the following geometry: $\xi = 0°$, $\chi = -28°$. Fig. 5 illustrates the (σ, π) components of the electric field E generated by the quarter-wave plate and how the monochromator crystal analyzer has to be rotated in order to have a pure π' component and no intensity be transmitted by the analyzer.

3.2. *Results and discussion*

These predictions were fully confirmed by our experiments which were conducted in a slightly different way. In the perspective of further refinements of the quantitative analyses, we found it desirable to record, for every different angular set-up $R_s(\chi)$ of the analyzer, the whole transmission profile $I(\Delta\Theta)$ which may be obtained on scanning the angular offset $\Delta\Theta$ of the quarter-wave plate over the range of interest, *i.e.* −300 arcsec, +300 arcsec. Indeed, as illustrated in Figs. 6(*a*) or 6(*b*), there is a clear minimum in the transmitted intensity that appears for the predicted angular offset of $\Delta\Theta = -50$ arcsec. Note that, as easily anticipated from Fig. 4, completely flat transmission profiles were observed when both the quarter-wave plate and the analyzer were set at the reference positions, *i.e.* $r_s(\xi = 0°)$ and $R_s(\chi = 0°)$, or, more generally, whenever the condition $r_s(\xi) = R_s(\chi)$ held true. This is because at $\theta_B \simeq 45°$, only the σ' component of the analyzer can contribute to the transmitted signal and the geometrical configuration implies that the σ' component is nothing more than the π component of the circularly polarized radiation incident on the quarter-wave plate: Fig. 4 clearly shows that $I_\pi(\Delta\Theta)$ is completely flat and this dependence is simply reproduced by the analyzer.

At this stage one may raise the question of why the minimum intensity does not drop off to zero in the experimental profile reproduced either in Fig. 6(*a*) or 6(*b*). It would be premature to speculate about the polarization state of the incident radiation on the quarter-wave plate without first taking into account other interpretations for the observed damping of the extrema in the transmission profiles:

(i) transmission profiles have to be convolved with the finite divergence of the incident beam, which is not negligible in the horizontal plane;

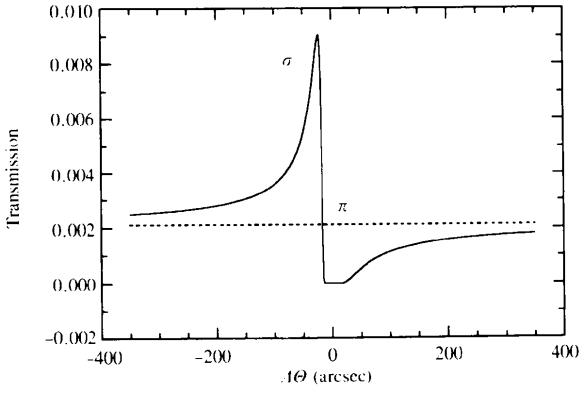

Figure 4
Transmission coefficient calculated for the σ (full line) and π (dotted line) components of the electric field as a function of the angular offset $\Delta\Theta$ of the phase plate. In this calculation we have considered a symmetric 111 reflection in Bragg geometry and we have assumed that the thickness of the plate is 16 μm and that the energy is 2.836 keV.

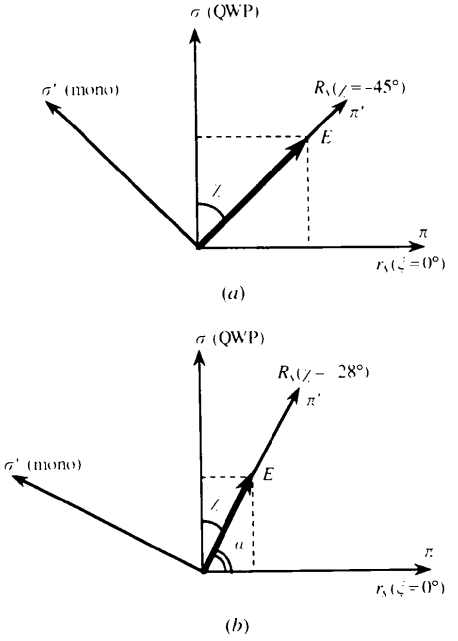

Figure 5
Sketches representing the (σ, π) axes of the quarter-wave plate and the (σ', π') axes of the monochromator crystal analyzer assuming (*a*) identical transmission of the (σ, π) components of the electric field E, and (*b*) different transmission of the (σ, π) components of the electric field E. Note that the monochromator has to be rotated by $\chi = \alpha - 90°$ in order to allow the electric field E to have a pure π' component and no transmitted intensity by the monochromator crystal analyzer.

(ii) thermomechanical deformations of the thin crystal under a high heat load were observed to cause unexpected broadening of the diffraction profiles;

(iii) there may be some residual unwanted background due, for instance, to scattering tails of the diffraction profiles in the monochromator or, possibly, to the presence of residual amounts of harmonics.

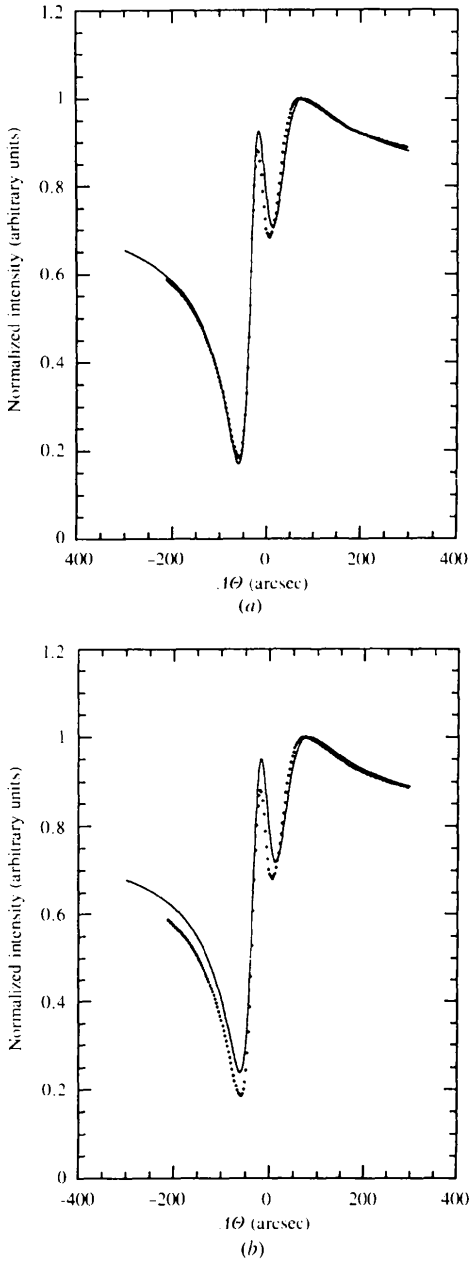

Figure 6
Sensitivity of the fit *of the same experimental data* (dotted lines) with theoretical simulations (full lines) carried out assuming *two different* values for the circular polarization rate P_3 of the source. The intensity transmitted by the monochromator–analyzer as a function of the angular offset $\Delta\Theta$ of the phase plate is measured or calculated. The diffraction planes are (i) *horizontal* for the phase plate (*i.e.* $\xi = 0°$); (ii) inclined at 28° with respect to the vertical plane for the analyzer (*i.e.* $\chi = -28°$). All fits were generated with the basic assumption that the incident beam is a plane wave and on convolving the final result with a Gaussian of 35 arcsec FWHM. (*a*) $P_3 = 0.97$; (*b*) $P_3 = 0.90$.

With a little bit of time and effort we found it possible to fit the experimental profiles $I(\Delta\Theta)$ against a simple theoretical model requiring a minimum number of adjustable parameters, *i.e.* the polarization rate of the source $P_3 = s_3/s_0$, the crystal thickness ($e = 16\ \mu m$) and a Gaussian broadening of the diffraction profile with typically 35 arcsec FWHM (to be compared with the theoretical value of the monochromator Darwin width of 30 arcsec). We found it preferable to subtract a small background amounting to $\leq 5\%$ of the intensity measured outside the transmission profile. Let us recall here that we could not use the four-mirror device for these early experiments: the practical consequence was that a fairly intense signature of the third-order harmonics did show up in the 'rocking curves' measured with the double-crystal monochromator. Actually, we suspect that even though the parallelism of the two crystals of the monochromator was deliberately offset, we could not completely eliminate a small residual contamination with the tails of unwanted harmonics which are detected with a higher efficiency by a photodiode. In our opinion a contamination by residual harmonics and/or by scattering tails may perfectly well justify the subtraction of a small background. With the mirrors we already know that the harmonics rejection can be improved by several orders of magnitude, but scattering tails cannot be eliminated that easily. Thus, background subtraction may still be necessary for experiments carried out with the mirrors and, in the future, this could remain a sensible limitation regarding the accuracy of the method.

Nevertheless, as illustrated in Fig. 6(*a*), there is a remarkable agreement between the experimental data and a simulated transmission profile generated under the assumption that $P_3 = 97\%$. Obviously, this is very encouraging even though the fit is not perfect everywhere. Given the experimental limitations, we felt it unrealistic to refine the P_3 value any further as it seems difficult to set precise error bars. For the sake of comparison, we decided to reproduce (Fig. 6*b*) the best fit obtained when the simulated transmission profile is generated with a lower polarization rate of the source, *i.e.* $P_3 = 90\%$: clearly the differences between the experimental and simulated profiles are significantly increased. A series of tentative fits led us to the conservative conclusion that the circular polarization rate of the source should be in the range: $95 \leq P_3 \leq 100\%$. This is in good agreement with the theoretical predictions made earlier for this helical undulator (Elleaume, 1994).

The analysis is clearly limited by the difficulty in making reasonable guesses for the thickness of the phase plate and for the width of the Gaussian used to convolve the calculated transmission profiles. In this respect, more attention should be paid to the extra peak that is observed near $\Delta\Theta = 0$ in all profiles recorded with $r_s(\xi = 0°)$ and $R_s(\chi = -28°)$. This extra peak is related to the maximum of $I_\sigma(\Delta\Theta)$ in Fig. 4 and is critically sensitive to the thickness of the plate:

it gave us an additional way of assessing the consistency of the estimated thickness of 16–17 μm.

In conclusion, we have established the feasibility of X-ray polarimetry with a quarter-wave plate at energies as low as 2.8 keV. The originality of the approach described in the present paper stems from two major points:

(i) The quarter-wave plate was inserted upstream of the monochromator which is then used not only as a monochromator but also as a linear polarimeter since the Bragg angle is close to 45°. This experimental configuration has the clear advantage that the polarization state of the undulator radiation can be measured without any alteration caused by the monochromator.

(ii) We have monitored the changes in intensity of the σ' component of the electric field diffracted by the monochromator as a function of the angular offset of the phase plate. In other words, we scanned the phase shift induced by the phase plate for a fixed orientation of the linear analyzer. This method proved to be more sensitive than the conventional approach which consists of analyzing the linear polarization of the beam by rotating the analyzer when the phase plate is operated as a true quarter-wave plate.

The quality of the fits looks extremely encouraging and also confirms the excellent circular polarization rate of the source. In future experiments mirrors should be systematically inserted in order to filter out the small residual background due to harmonics. Also, the temperature control of the thin crystal needs to be improved.

APPENDIX *A*
Geometrical effects induced by R_s rotations of the monochromator

In practice, axial rotations $R_s(\chi)$ of the monochromator were found to be quite sensitive to small defects in the alignment of the beamline or in the tuning of the monochromator itself. This is due to geometrical effects which are briefly analyzed below and can be used ultimately to optimize the operation of the beamline.

*A*1. Incorrect calibration in energy

Let $\mathbf{k}$ be the wavevector of the incident photons, and let $\mathbf{h}_1$ and $\mathbf{h}_2$ be the normals to the diffracting planes of the first and second crystal of the monochromator, respectively. By definition we will consider that: $\mathbf{h}_1$ is obtained by transforming the unit vector $\mathbf{u}_1$ [0,0,$\bar{1}$] according to the successive rotations $\mathbf{R}_y$ $(-\theta)$ and $\mathbf{R}_y$ $(+\chi)$; $\mathbf{h}_2$ is obtained by transforming the unit vector $\mathbf{u}_2$ [0,0,1] according to the successive rotations $\mathbf{R}_y$ $(-\theta')$ and $\mathbf{R}_y$ $(\chi + \Delta\chi)$; and $\mathbf{k}$ is obtained by transforming the unit vector $\mathbf{s}$ [0,1,0] according to the successive rotations $\mathbf{R}_x$ $(+\eta)$ and $\mathbf{R}_y$ $(+\psi)$.

For the vectors $\mathbf{h}_1$ and $\mathbf{h}_2$, rotations $\mathbf{R}_y$ and $\mathbf{R}_y$ are quite natural and can be really produced with the mechanics of the monochromator, whereas for the wavevector $\mathbf{k}$, such rotations are indeed fully artificial and are introduced to locally describe the consequences of a frozen misalignment of the beam axis. Note that $\Delta\chi$ is a small angular offset in the parallelism of the second crystal and has nothing to do here with any differential rotation of the first crystal around the y axis. Next, on formulating the relevant rotation matrices, one is led without any ambiguity to the following result:

$$\mathbf{k}\begin{bmatrix}+\sin\psi\sin\eta\\ +\cos\eta\\ +\cos\psi\sin\eta\end{bmatrix},\quad \mathbf{h}_1\begin{bmatrix}-\sin\chi\cos\theta\\ -\sin\theta\\ -\cos\chi\cos\theta\end{bmatrix},$$

$$\mathbf{h}_2\begin{bmatrix}\sin\chi\cos\theta' + \cos\chi\cos\theta'\,\Delta\chi\\ \sin\theta'\\ \cos\chi\cos\theta' - \sin\chi\cos\theta'\,\Delta\chi\end{bmatrix}.$$

The beamline is perfectly aligned whenever $\eta = 0$, with the practical consequence that ψ becomes undefined. This may not necessarily be the case and, then, the energy calibration of the monochromator will become geometry dependent. In order to show this, one simply needs to calculate the following dot products:

$$-\mathbf{k}\cdot\mathbf{h}_1 = \sin\theta\cos\eta + \cos\theta\sin\eta\cos(\psi - \chi) = \sin\theta_1 \quad (3)$$

$$-\mathbf{k}'\cdot\mathbf{h}_2 = \sin\theta_1 - \cos\theta\,[\sin\eta\sin(\psi - \chi)\Delta\chi + \cos\eta\,\Delta\theta] + \sin\theta\,[\sin\eta\cos(\psi - \chi)\Delta\theta] = \sin\theta_2. \quad (4)$$

where we have used the simplifying notation $\theta' = \theta + \Delta\theta$. If the beamline was perfectly aligned ($\eta \to 0$), then the adjustment of $\Delta\theta$ and $\Delta\chi$ could be completely uncorrelated: this is unfortunately not always the case and (4) implies that if $\eta \neq 0$ then the rocking curve, *i.e.* $\Delta\theta$, has to be re-adjusted in order to match the condition $\sin\theta_1 = \sin\theta_2$ and maximize the transmitted intensity every time $\Delta\chi$ is changed. This is indeed confirmed experimentally and this clearly has nothing to do with any imperfection in the mechanical design of the monochromator but with alignment problems. To the first order in $\sin\eta$, the matching condition is simply:

$$\Delta\theta = -\Delta\chi\sin\eta\sin(\psi - \chi). \quad (5)$$

Next, let us use a Taylor expansion of $\sin\theta_1$ to the first order:

$$\sin\theta_1 = \sin\theta + \cos\theta\,\Delta\theta_1$$

with

$$\Delta\theta_1 = \sin\eta\cos(\psi - \chi). \quad (6)$$

One may thus predict a significant shift of the energy calibration given by:

$$\Delta E/E = -\text{cotan}\,\theta\,\Delta\theta_1 \simeq -\text{cotan}\,\theta\sin\eta\cos(\psi - \chi). \quad (7)$$

This result confirms that the experiment, as expected, is

most sensitive to any small misalignment in the vertical plane contributing to $\eta \neq 0$. Under such conditions any axial rotation $R_s(\chi)$ will cause an energy shift proportional to $\cos(\psi - \chi)$. Such typical behaviour is illustrated in Fig. 7, where a fit with a cosine function yields a small value for the angular offset $\psi \simeq -3.6°$. The amplitude of the cosine function is related to the critical parameter η which, in this particular example, was found to be of the order of 7.6 arcmin. Such a large misalignment can be easily understood since the corresponding test measurement was carried out when the four-mirror device was inserted for the first time and was not yet perfectly adjusted. Such a test appears as a very critical way of aligning the four-mirror device.

A2. Adjustment of the χ-parallelism of the two crystals

A sensitive alignment procedure has been developed which makes use of a beam-position monitor (BPM2) located behind the monochromator (see Fig. 1) at a distance D from the first crystal. The first step is to write the components of the exit wavevector $\mathbf{k}_{out}$ using the basic equation

$$\begin{aligned}\mathbf{k}_{out} &= \mathbf{k} - 2(\mathbf{h}_1\cdot\mathbf{k})\mathbf{h}_1 - 2(\mathbf{h}_2\cdot\mathbf{k}')\mathbf{h}_2 \\ &= \mathbf{k} + 2\sin\theta_1(\mathbf{h}_1 + \mathbf{h}_2),\end{aligned} \tag{8}$$

where we have again assumed that the condition, $\sin\theta_2 = \sin\theta_1$, was fully satisfied. One would then obtain the following expression of $\mathbf{k}_{out}$:

$$\mathbf{k}_{out} = \begin{bmatrix} \sin\psi\sin\eta + \sin 2\theta\cos\chi\,\Delta\chi + [(\cos 2\theta \\ \quad + \cos 2\chi)\cos\psi + \sin 2\chi\sin\psi]\sin\eta\,\Delta\chi \\ \cos\eta \\ \cos\psi\sin\eta + \sin 2\theta\sin\chi\,\Delta\chi - [(\cos 2\theta \\ \quad - \cos 2\chi)\sin\psi + \sin 2\chi\cos\psi]\sin\eta\,\Delta\chi \end{bmatrix} \tag{9}$$

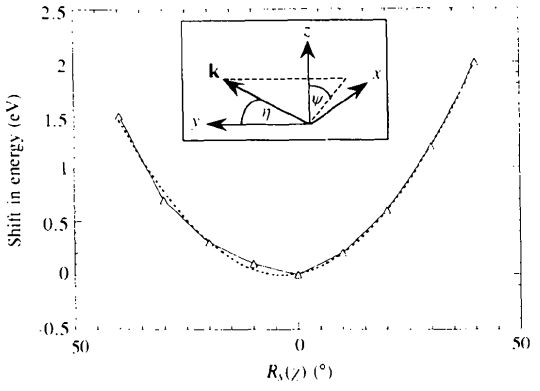

Figure 7
Detected shift in the energy calibration of the monochromator on scanning the azimuthal angle χ in the case where the incident beam **k** did not exactly coincide with the mechanical rotation axis y. The inset shows the coordinate system used for the calculations of *Appendix A*.

For simplicity, we will hereafter neglect all 'second-order terms' $\propto \sin\eta\Delta\chi$. The coordinates $[X, Z]$ of the exit beam at the beam-position-monitor location can now be easily calculated:

$$X = d_{offset}\sin\chi + D(\sin\psi\tan\eta + \sin 2\theta\cos\chi\,\Delta\chi), \tag{10}$$

$$Z = d_{offset}\cos\chi + D(\cos\psi\tan\eta - \sin 2\theta\sin\chi\,\Delta\chi), \tag{11}$$

where d_{offset} refers to the vertical offset of the exit beam (*i.e.* −12.5 mm) induced by the double-crystal monochromator.

In practice, it may be more convenient to use symmetric and antisymmetric combinations of the beam coordinates with respect to the +/− sign of the rotations $R_s(\pm\chi + \chi_0)$, where it is implicitly assumed that there may be some (undesired) constant offset χ_0 biasing the definition of χ:

$$\begin{aligned}(X^+ + X^-) = {} & 2D(\sin 2\theta\cos\chi\cos\chi_0\,\Delta\chi + \sin\psi\tan\eta) \\ & + 2d_{offset}\cos\chi\sin\chi_0,\end{aligned} \tag{12}$$

$$\begin{aligned}(X^+ - X^-) = {} & -2D(\sin 2\theta\sin\chi\sin\chi_0\,\Delta\chi) \\ & + 2d_{offset}\sin\chi\cos\chi_0,\end{aligned} \tag{13}$$

$$\begin{aligned}(Z^+ + Z^-) = {} & -2D(\sin 2\theta\cos\chi\sin\chi_0\,\Delta\chi + \cos\psi\tan\eta) \\ & + 2d_{offset}\cos\chi\cos\chi_0,\end{aligned} \tag{14}$$

$$\begin{aligned}(Z^+ - Z^-) = {} & -2D(\sin 2\theta\sin\chi\cos\chi_0\,\Delta\chi) \\ & - 2d_{offset}\sin\chi\sin\chi_0.\end{aligned} \tag{15}$$

We expect the maximum sensitivity of $\Delta\chi$ to be obtained for $\theta \simeq 45°$ because $\sin 2\theta \simeq 1$. One may also note that, for $\chi = 45°$, $(X^+ - X^-)$ and $(Z^+ + Z^-)$ should be strictly identical, whereas $(X^+ + X^-)$ and $(Z^+ - Z^-)$ should have opposite signs, if and only if the beamline is well aligned ($\eta \to 0$). It is also worth noting that (12) and (15) inherently have a rather weak sensitivity to the angular offset χ_0. This is because the distance D (≥ 2 m) is much larger than d_{offset} (12.5 mm). Let us emphasize that there is a quantity that is strictly independent of any angular offset χ_0:

$$\begin{aligned}(X^+ - X^-)^2 + (Z^+ - Z^-)^2 = {} & 4(\sin\chi)^2[d_{offset}{}^2 \\ & + (D\sin 2\theta\,\Delta\chi)^2].\end{aligned} \tag{16}$$

The authors are very grateful to Dr A. Freund (ESRF Optics group) who supported this project from the beginning and gave us free access to the ESRF crystal laboratory. A special acknowledgement should be made to A. Paul and J. P. Vassali who cut all the crystals and took care of the critical etching step in the fabrication of the thin quarter-wave plate. Their skill simply made this difficult project feasible. Special thanks are also due to Dr P. Elleaume and Dr J. Chavanne who were in charge of the design and construction of the helical undulators Helios-I and Helios-II used on the ID12 section of the ESRF storage ring.

References

Belyakov, V. A. & Dmitrienko, V. E. (1989). *Sov. Phys. Usp.* **32**, 697–719.

Chen, C. T. (1987). *Nucl. Instrum. Methods*, A**256**, 595–604.
Chen, C. T. & Sette, F. (1989). *Rev. Sci. Instrum.* **60**, 1616–1621.
Dmitrienko, V. E. & Belyakov, V. A. (1980). *Pis'ma Zh. Tekh. Fiz.* **6**, 1440–1441; *Sov. Techn. Phys. Lett.* **6**, 621–622.
Elleaume, P. (1994). *J. Synchrotron Rad.* **1**, 19–26.
Elleaume, P., Chavanne, J., Marechal, X., Goulon, J., Braicovich, L., Malgrange, C., Emerich, H., Marot, G. & Susini, J. (1991). *Nucl. Instrum. Methods*, A**308**, 382–389.
Gauthier, C., Goujon, G., Feite, S., Moguiline, E., Braicovich, L., Brookes, N. B. & Goulon, J. (1995). *Physica*, B**208/209**, 232–234.
Giles, C., Malgrange, C., De Bergevin, F., Goulon, J., Baudelet, F., Fontaine, A., Vettier, C. & Freund, A. (1995). *Nucl. Instrum. Methods*, A**361**, 354–357.
Giles, C., Malgrange, C., Goulon, J., De Bergevin, F., Vettier, C., Dartyge, E., Fontaine, A., Giorgetti, C. & Pizzini, S. (1994*a*). *J. Appl. Cryst.* **27**, 232–240.
Giles, C., Malgrange, C., Goulon, J., De Bergevin, F., Vettier, C., Dartyge, E., Fontaine, A., Giorgetti, C. & Pizzini, S. (1994*b*). *Nucl. Instrum. Methods*, A**349**, 622–625.
Giles, C., Malgrange, C., Goulon, J., De Bergevin, F., Vettier, C., Dartyge, E., Fontaine, A., Pizzini, S., Baudelet, F. & Freund, A. (1995*a*). *Rev. Sci. Instrum.* **66**, 1549–1553.
Giles, C., Malgrange, C., Goulon, J., De Bergevin, F., Vettier, C., Dartyge, E., Fontaine, A., Pizzini, S., Baudelet, F. & Freund, A. (1995*b*). *Physica*, B**208/209**, 784–786.
Giles, C., Malgrange, C., Goulon, J., Vettier, C., De Bergevin, F., Freund, A., Elleaume, P., Dartyge, E., Fontaine, A., Giorgetti, C. & Pizzini, S. (1993). *Proc. SPIE*, **2010**, 136–149.
Giles, C., Vettier, C., De Bergevin, F., Malgrange, C., Grübel, G. & Grossi, F. (1995). *Rev. Sci. Instrum.* **66**, 1518–1521.
Hart, M. & Lang, A. R. (1965). *Acta Cryst.* **19**, 73–77.
Hirano, K., Ishikawa, T. & Kikuta, S. (1995). *Rev. Sci. Instrum.* **66**, 1604–1609.
Hirano, K., Izumi, K., Ishikawa, T., Annaka, S. & Kikuta, S. (1991). *Jpn J. Appl. Phys. Lett.* **30**, L407–410.
Hirano, K., Kanzaki, K., Mikami, M., Miura, M., Tamasaku, K., Ishikawa, T. & Kikuta, S. (1992). *J. Appl. Cryst.* **25**, 531–535.
Ishikawa, T., Hirano, K., Kanzaki, K. & Kikuta, S. (1995). *Rev. Sci. Instrum.* **66**, 1098–1103.
Ishikawa, T., Hirano, K. & Kikuta, S. (1991). *J. Appl. Cryst.* **24**, 982–986.
Lang, J. C. & Srajer, G. (1995). *Rev. Sci. Instrum.* **66**, 1540–1542.
Malgrange, C., Carvalho, C., Braicovich, L. & Goulon, J. (1991). *Nucl. Instrum. Methods*, A**308**, 390–396.
Matsushita, T., Ishikawa, T. & Oyanagi, H. (1986). *Nucl. Instrum. Methods*, A**246**, 377–386.
Molière, G. (1939). *Ann. Phys. (Leipzig)*, **35**, 272–313.
Skalicky, P. & Malgrange, C. (1972). *Acta Cryst.* A**28**, 501–507.